Journal of Solid State Chemistry **167,** 425–434 (2002)
doi:10.1006/jssc.2002.9649

# Crystallite Nanosize Effect on the Structural Transitions of $WO_3$ Studied by Raman Spectroscopy

M. Boulova* and G. Lucazeau†,[1]

*Chemistry Department, Moscow State University, Moscow 119899, Russia; and †Laboratoire d'Électrochimie et de Physico-Chimie des Matériaux et des Interfaces, INPG-CNRS, 1130 rue de la Piscine, BP75, 38402 St Martin d'Hères Cedex, France

Received December 2, 2001; in revised form April 17, 2002; accepted May 10, 2002

**Nanocrystallites of tungsten oxide samples of 2, 4, 16, 35 and 60 nm of diameter were prepared by cryosol and pyrosol techniques. The pressure- and temperature-induced phase transitions of these samples were monitored by Raman spectrometry from 0.1 MPa to 34 GPa and from 77 to 1200 K. The tetragonal ($\alpha$)–orthorhombic ($\beta$)–monoclinic ($\gamma$) transitions in these nanometric samples are strongly downshifted in temperature by comparison with the bulk $WO_3$. For instance, the tetragonal phase which exists above 1171 K for the bulk tungsten oxide can be stabilized at 700 K for the 35 nm sample. In the same way, the monoclinic $P2_1/n$-monoclinic $P2_1/c$ high-pressure-induced transition is slightly shifted from 0.1 GPa to a higher pressure (1.5 GPa). The discussion of these transition-line shifts is based on thermodynamic considerations in which the surface energy of crystallites plays an important role.** © 2002 Elsevier Science (USA)

*Key Words:* **tungsten oxide; nano-crystalline materials; phase transition; Raman spectroscopy; high pressure.**

## I. INTRODUCTION

As mentioned in Ref. (1), the properties of nanostructured materials deviate from those of single crystals (or coarse-grained polycrystals) with the same average chemical composition. This deviation results as well from the reduced size and/or dimensionality of the nanometer-sized crystallites as from the numerous interfaces between adjacent crystallites. An elaboration of nanometric-oxides-based gas sensors (such as nanocrystallized tungsten oxide) (2–6) functioning under different conditions (temperature, pressure, humidity, etc.) needs to determine and to separate the structural changes induced by the temperature and pressure influence on the nanocrystalline oxide from the gas influence by itself. Thus, the knowledge of the phase diagram of different nanometric samples of $WO_3$ is an important first step.

There is abundant literature on the structure of bulk or microcrystallized $WO_3$. The sequence of temperature-induced phase transitions for bulk microcrystallized $WO_3$ is the following: monoclinic $Pc$ ($\varepsilon$-$WO_3$) $\xrightarrow{230\,K}$ triclinic $P\bar{1}$($\delta$-$WO_3$) $\xrightarrow{300\,K}$ monoclinic $P2_1/n$ ($\gamma$-$WO_3$) $\xrightarrow{623\,K}$ orthorhombic $Pnma$ ($\beta$-$WO_3$) $\xrightarrow{1020\,K}$ tetragonal $P4/ncc$ ($\alpha$-$WO_3$) $\xrightarrow{1171\,K}$ $P4/nmm$ (see Table 1) (7–11).

In our previous studies (12, 13) from the high-pressure Raman and X-ray studies of microcrystallized tungsten oxide, it was concluded to the existence of two first-order phase transitions (at 0.1 GPa towards monoclinic $P2_1/c$ form ($HP1$) and at 22 GPa towards another monoclinic form ($HP4$)). Two small spectral anomalies were observed at about 3 ($HP2$) and 10 GPa ($HP3$), and were attributed to small structural changes.

The study of the effect of crystallite size on the physical and chemical properties of solids is an active topic. The temperature and the pressure of phase transitions are strongly shifted from the bulk to the nanometric states of a solid. The surface energy difference between the phases involved is mainly responsible for an increase in the transition pressure and the increase of the bulk modulus. In the same way, the surface energy is also involved in the Gibbs–Thomson expression of the downshift of the melting temperature of small crystallites. This expression was extended recently to nanometric zirconia for explaining the displacements of the phase transition lines in the $P$–$T$ diagram of these materials. For instance, by application of Gibbs–Thomson relation to solid–solid transition (14), the temperature lowering $\Delta T = 1400°$, observed for the monoclinic–tetragonal transition of a 7 nm zirconia could be reproduced by this relationship (15–17). Similar effects are expected for nanometric tungsten oxide. Thus, one of the aims of this work is to estimate the surface energy of

[1] To whom correspondence should be addressed. Fax: +33-04-76-82-66-30. E-mail: guy.lucazeau@lepmi.inpg.fr.



0022-4596/02 $35.00

**TABLE 1**
**Structural Data as Reported in the Literature**

| Ref. (10) | | Ref. (27) | | |
|---|---|---|---|---|
| Phase | Transition temperature (K) | Phase | Transition temperature (K) | Structural notation |
| *P*4/*nmm* | | | | |
| | 1170 | | | |
| *P*4/*ncc* | | *P*4/*ncc* | | |
| | 1000 | | 1073 | α |
| $P\bar{4}2_1m$ | | | | |
| *Cmca* | | | | |
| | | | | β |
| *Pnma* | | *Pbcn* | | |
| | 600 | | 623 | |
| $P2_1/n$ | | | | γ |
| $P\bar{1}$ | | | | δ |
| | 230 | | | |
| *Pc* | | | | ε |

crystallites from the shift of the temperature and pressure of the transitions due to the reduction of the crystallites size. The knowledge of this quantity will be useful in the analysis of the chemical reactivity of nanometric samples.

The present work is a contribution to a systematic study of the effect of the crystallite size on the pressure- and temperature-induced phase transitions that we have undertaken on oxides. The investigated pressure and temperature ranges were below 34 GPa and 1200 K, respectively. A parallel study of the nanosize effect on their reactivity towards different gases is also undertaken (6).

## II. EXPERIMENTAL

Nanocrystalline powders of $WO_3$ were prepared according to two different routes. The first one consists in the treatment of a $(NH_4)_{10}W_{12}O_{41}$ aqueous solution in $H^+$-resin. The resultant colloidal solution is then freeze dried in a sublimator. Crystallite size obtained by this method was estimated equal to about 2 nm (see below). The second route was the spray-pyrolysis method already described in Ref. (18). The aerosol of $(NH_4)_{10}W_{12}O_{41}$ aqueous solution was decomposed at three different temperatures (400°C, 600°C and 900°C) in order to obtain powders of different grain size (4, 35, and 60 nm, respectively). Thermogravimetric analysis (TGA) measurements show that the 2 nm sample loses 1.1 mol $H_2O/WO_3$ above 360°C, while the water content of the 4 nm sample is about 0.3 $H_2O$. No water content was detected for the 35 and 60 nm samples.

The 16 nm crystallites sample was obtained by heating the 4 nm sample in a close cell. The mass of substance was not sufficient for X-ray diffraction measurements and the crystallite size was estimated from the wavenumber of the Raman band at about 265 $cm^{-1}$ which increases approximately linearly from 263 $cm^{-1}$ for 4 nm to 268 and 275 $cm^{-1}$ for 35 and 60 nm samples, respectively (i.e., about 6 nm/$cm^{-1}$). The same sample was also obtained by repetitive heating of the 4 nm sample under laser for a few seconds in order to perform a quenching similar to that of

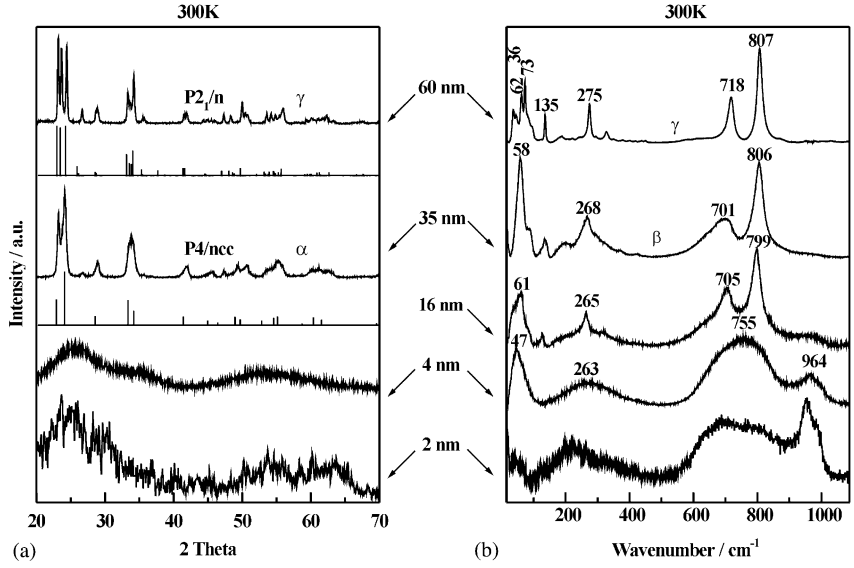


**FIG. 1.** As-obtained 2, 4, 35, and 60 nm samples at room temperature, the 16 nm sample was obtained by thermal treatment of the 4 nm sample. (a) X-ray diffraction diagrams, the theoretical positions of diffraction lines for the γ- and α-forms are plotted on the diagrams and (b) Raman spectra. The baseline and the Rayleigh contribution in Raman spectra are subtracted.

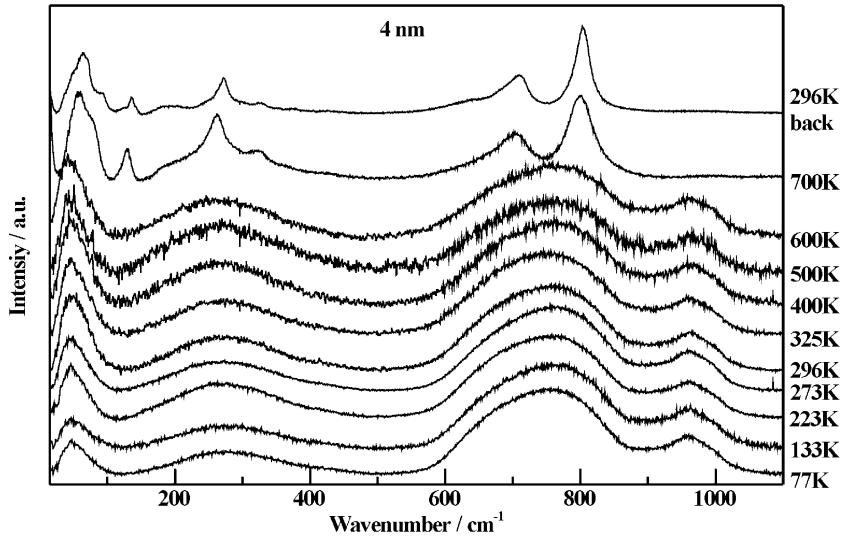


**FIG. 2.** Temperature effect on the 4 nm sample: crystallites growth and transformation into $\beta$-phase.

the pyrosol process followed by a subsequent spectral control under a low laser power excitation. This process was interrupted when the spectrum was found close to the one considered as representative of the $16(\pm 5)$ nm size. The water content of this sample was not determined by TGA, but no OH bands were detected for this sample.

X-ray diagrams were obtained on a Siemens D500 diffractometer at room temperature. The volume-weighted average crystallite sizes were deduced from X-ray diffraction diagrams using the Scherrer formula (19): $d = K\lambda/\beta\cos\theta$, where $d$ is the diameter of the crystallites (in the approximation of a spherical shape), $K = 0.9$, $\lambda(\mathrm{Cu}K\alpha) = 1.54051$ Å, and $\beta$ is the breadth of the diffraction lines.

The diffractogram of the 60 nm sample is mainly representative of the $\gamma$-phase and the corresponding parameters were refined with the Xfit software and found equal to $a = 7.3043$ Å, $b = 7.5313$ Å, $c = 7.6833$ Å $\beta = 90.7645$. In addition, a Williamson–Hall (20) plot of $B_L\cos\theta$ versus $\sin\theta$ for the 11 first lines has shown that there is practically zero contribution of stresses to the broadening of lines. The 35 nm diffractogram corresponds to the $\alpha$-phase and the parameters $a = 5.2386$ Å and $c = 7.6670$ Å were obtained.

Notice that for the smallest crystallite sizes obtained in the present work, the X-ray diagram is made of broad-bands and thus the determination of the corresponding size values is very approximate.

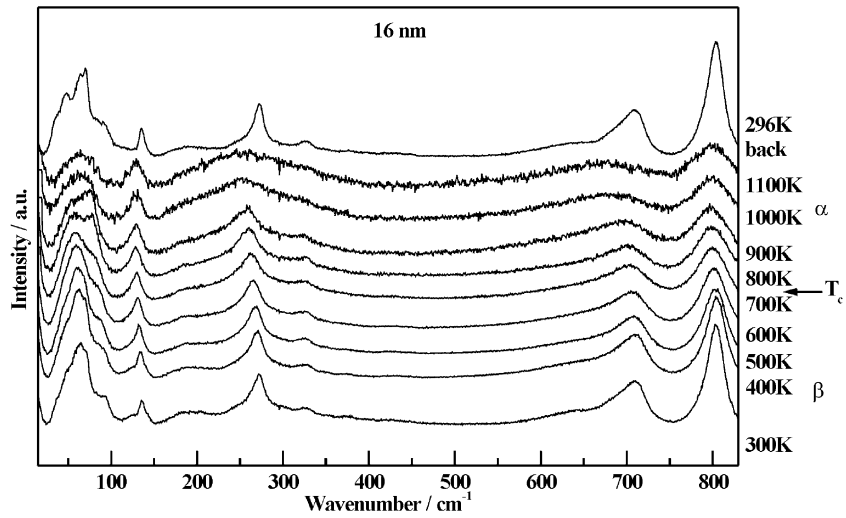


**FIG. 3.** Temperature effect on the 16 nm sample: $\beta$–$\alpha$ transition.

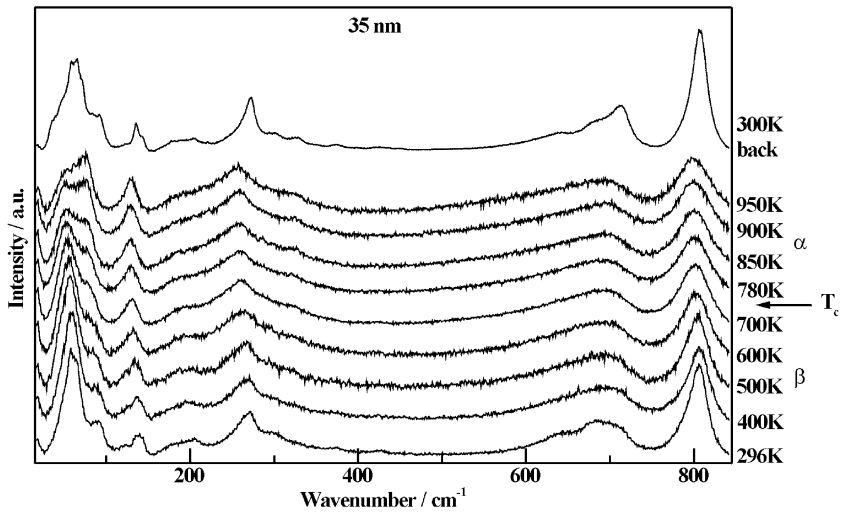


**FIG. 4.** Temperature effect on the 35 nm sample: $\beta$–$\alpha$ transition.

The reference spectra presented further were performed on a sample of microcrystallized (500 nm) $WO_3$ obtained from Aldrich.

Raman spectra were obtained using a backscattering geometry on a XY Dilor multi-channel spectrometer equipped with a CCD detector. The 514.53 nm line from an argon ion laser was used as the excitation source. Incident powers ranging between 0.3 and 5 mW on the sample were used.

For high-pressure measurements, the sample was placed in a diamond anvil cell (DAC) in which inconel gasket was used as the sample chamber. A mixture of 4:1 ethanol–methanol and nujol were used as pressure-transmitting media. Nujol was preferred for hydrated samples for avoiding any interaction of the hydration water of the sample with alcohol. A second type of pressure investigation consisted in studying the powder without transmitting medium; i.e., the gasket was filled completely with powder. In both types of experiments, small fragments of ruby were mixed to the sample in order to use ruby fluorescence lines as internal indicators of the applied pressure (21). In our previous study on the 500 nm Aldrich sample, similar conditions were achieved and the unexpected quasi-hydrostaticity observed up to 30 GPa was related to its exceptional small bulk modulus. After focusing with a $\times 20$ microscope objective, the laser spot was about 2 μm in diameter.

## III. RESULTS

Figure 1 represents the room temperature X-ray diffractograms and the Raman spectra of different samples in their initial state.

Figures 2–4 and 6 represent the temperature effect on the Raman spectra of the 4, 16, 35 and 60 nm samples. The 4 nm sample is stable up to 600 K, at 700 K the broadband at 800 $cm^{-1}$ splits into two components and the high-frequency band at about 950 $cm^{-1}$ disappears. This spectral change is related to the departure of water (even in close vessel), and to the growth of crystallites (see further). The final spectrum after returning to 300 K is characteristic of the 16 nm sample. No spectral changes are

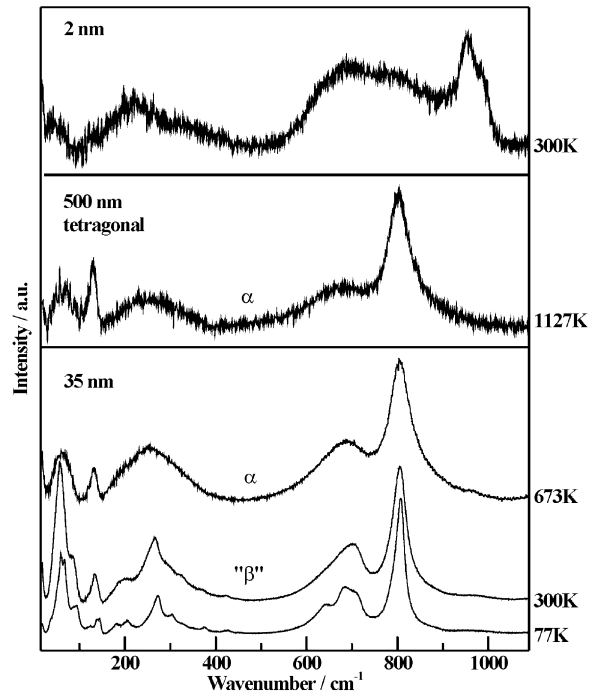


**FIG. 5.** Comparison between spectra obtained at 1127 K for the bulk sample and at 673 K for the 35 nm sample, both spectra correspond to the $\alpha$ tetragonal structure. The spectrum of the 2 nm sample at 300 K is also represented.

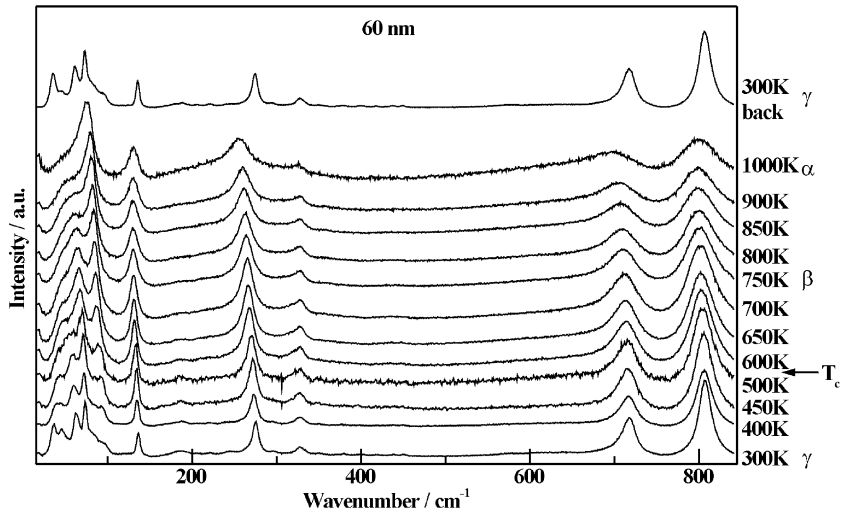


**FIG. 6.** Temperature effect on the 60 nm sample: $\gamma$–$\alpha$ transition and crystallites growth.

observed in the 77–300 K range for the 2 nm sample, above 300 K it starts to lose some water and its spectrum evolves continuously towards the spectrum of the 4 nm sample and for this reason its evolution is not represented. Figure 3 represents the spectral changes for the 16 nm sample resulting from a reversible structural change at about 800 K. Figure 4 represents the spectral changes resulting from a reversible structural change at about 900 K for the 35 nm sample. Figure 5 compares the high-temperature spectra of the 500 and 35 nm samples. The spectrum of the 2 nm sample at room temperature is also represented for showing the similarities between these samples. Figure 6 represents the spectra of the 60 nm sample; the change which occurs at about 550 K is reversible while the one above 1000 K results both from a structural change and from crystallite growth. The reference spectra presented in Fig. 7 are those of the 500 nm microcrystallized sample. The pressure-induced structural changes were obtained and discussed in a recent study (12, 13). The temperature-induced spectra have been obtained in the present work and agree with those of the literature (22–26). Figure 8 gives a schematic representation of the evolution of the transition temperatures with the size of crystallites.

The high-pressure Raman spectra of the 4 and 35 nm samples under hydrostatic and non-hydrostatic conditions

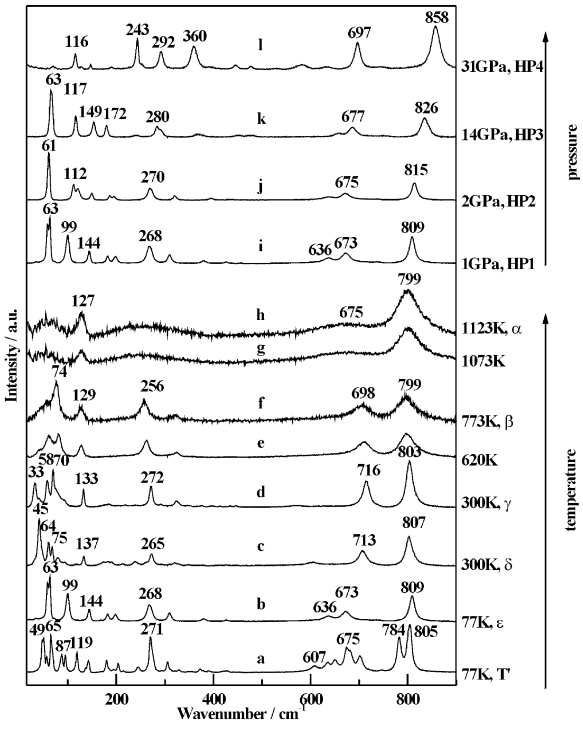


**FIG. 7.** Spectra of the 500 nm bulk $WO_3$ in different structural states obtained by varying the temperature and pressure.

| 500 nm | 60 nm | 35 nm | 16 nm | 4 nm 2 nm |
|---|---|---|---|---|
| α | α | α | α | "α" |
| 1171K | 950K | 800K | 700K | |
| β | β | "β" | "β" | |
| 623K | 550K | | | |
| γ | "γ" | | | |

**FIG. 8.** Crystallites size effect on temperature phase transition.

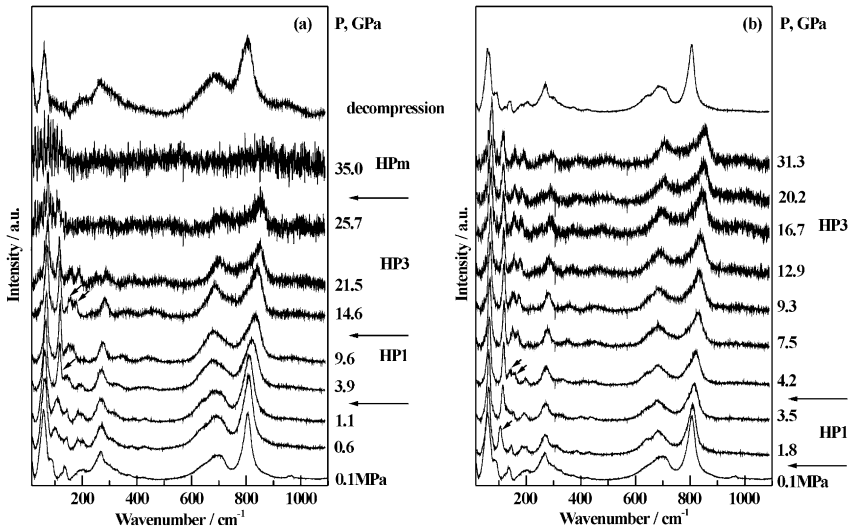


**FIG. 9.** Pressure dependence of the spectra of the 35 nm sample: (a) without pressure transmitting fluid: non-hydrostatic conditions and (b) in nujol: hydrostatic conditions. Small arrows indicate the bands which split or take intensity across a phase transition. *HPm* is a new phase (*m* is defined in the text).

are represented in Figs. 9 and 10. Different spectral changes are observed and will be discussed in terms of phase transitions. The reversibility of all the transformations was obtained.

## IV. DISCUSSION

### *A. Structural State of the Initial Samples (Fig. 1)*

The X-ray diagram of the 60 nm sample corresponds to the diffractogram of a pure $\gamma$-phase of $P2_1/n$ structure (25). In agreement with this conclusion, the corresponding Raman spectrum is quite similar to that of this $\gamma$-phase at 300 K reproduced in Fig. 7d. The X-ray diffractogram of the 35 nm sample is close to that of the $\alpha$-form of $P4/nnc$ structure which can be obtained from the neutron data of Ref. (27). The corresponding 300 K Raman spectrum with its strong low wavenumber band at 58 $cm^{-1}$ does not recall the spectrum of the $\alpha$-form given in Figs. 5 and 7h in which the lowest feature at about 50 $cm^{-1}$ is much weaker. The corresponding spectrum looks rather similar to that of the $\beta$-phase (Fig. 7f) assuming that the wavenumber of this mode decreases with the crystallite size as it is suggested by its downshift at 47 $cm^{-1}$ for the 4 nm sample. The $\delta$-phase ($P\bar{1}$ structure) spectrum (Fig. 7c) exhibits also some similitude with to that of the 35 nm spectrum, provided that all the bands of Fig. 7c are broadened. We shall see further, that under heating at 673 K, the 35 nm sample gives a spectrum quite identical to that of the $\alpha$-phase, showing that this structure has a clear Raman signature. Thus, at least at short range, the structure of the 35 nm sample at 300 K is probably close to that of the $\beta$-phase. The same conclusion can be proposed for the 16 nm sample. Finally, it must also be emphasized that the $\beta$-structure being close to the $\alpha$ one, the X-ray diffraction patterns are close to each other. Thus, it might be difficult in case of line broadenings to separate these structures by X-ray diffraction.

The 2 and 4 nm samples are clearly under an amorphous state, the broadbands as well in X-ray diffraction as in Raman scattering correspond to the envelope of the main lines of the different crystalline phases. Within the present model of size-dependent transition temperatures, this mixture of structures could originate from a broad dispersion of sizes of crystallites, each crystallite adopting a structure different from its neighboring one. However, the strong intensity decrease of the low-frequency mode for the 2 nm sample is the indication that it could be made of crystallites having rather the $\alpha$-structure (this state is noted "$\alpha$" in Fig. 8). At the same time, a new high-frequency mode at about 960 $cm^{-1}$ is observed and it grows in intensity when the crystallite size decreases. This could be due to vibrations of surface atoms, which become comparable in number with volume atoms for the 2 and 4 nm samples. It gains intensity when the crystallites size decreases. Analogous intensification of "surface" modes with the proportion of surface atoms was noticed for nanocrystalline tin oxide in Refs. (28–30) and for microcrystalline tungsten oxide during long milling (25). This band has completely disappeared in the 35 nm sample. The high wavenumber of these surface modes suggests that they involve dangling WO double bonds in weak interaction with water molecules (31).

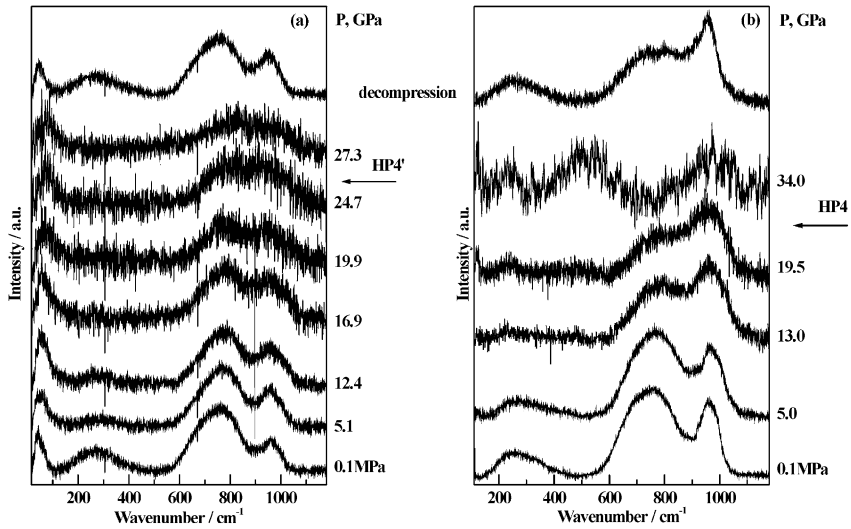


**FIG. 10.** Pressure dependence of the spectra of the 4 nm sample: (a) without pressure-transmitting fluid: non-hydrostatic conditions and (b) in nujol: hydrostatic conditions.

For small crystallite sizes, low-frequency modes were observed for different systems (32–35) and attributed to low acoustical modes characteristic of the mechanical eigenmodes of the nanometric crystallite as a whole. Their frequency varies like the reciprocal of the size of the particle ($\omega \approx L^{-1}$). Actually, the low-frequency band observed above 50 $cm^{-1}$ for the 2, 4 and even 16 nm samples rather increases with the crystallite size and corresponds to the numerous components of the bulk state and cannot reasonably be attributed to this kind of excitation.

## B. Temperature-Induced Phase Transitions

Figure 2 shows that temperature has practically no effect on the Raman spectra of the 4 nm sample between 77 and 600 K. The only change is the small intensification of the band at about 50 $cm^{-1}$ when the temperature is raised. The amplitude of this band normalized with the one at 800 $cm^{-1}$ reaches a maximum at about 300 K for the 4 nm sample. Above this temperature, as already mentioned, the crystallites start to grow but no structural changes can be evidenced, this fact reinforces the possibility for this sample to be in a structural state close to the α-form. The same considerations can be made for the 2 nm sample. The maximum intensity for the band at 50 $cm^{-1}$ is at about 250 K. However, this phenomenon is too small to conclude to a phase transition.

For the 16 nm sample, the low-frequency region of the spectrum starts to change at about 700 K, and it is probably due to the transition from β- to α-structure as it can be seen by a comparison with the 500 nm spectra in Figs. 7f and 7h. This transition takes place 471 K lower than the bulk $WO_3$. For the 35 nm sample, which can be heated up to 1000 K without losing its original crystallite characteristics, one observes changes in its Raman spectrum (Fig. 4) at about 800 K. All the bands become broader, the low-frequency mode at about 58 $cm^{-1}$ is strongly reduced and the loss of intensity for the whole spectrum is observed. This change can easily be attributed to the transformation towards the α tetragonal structure as shows the comparison with the spectrum of the bulk $WO_3$ heated at 1123 K in its tetragonal state (Fig. 5). Compared to the bulk $WO_3$, the transition is downshifted by 300 K. The 60 nm sample undergoes a first transition at 550 K probably from its γ-structure to the β one and a second transition towards the α-phase at about 950 K; however, the beginning of the crystallite growth process is observed simultaneously. Both transition temperatures have been downshifted by more than 100 K.

Note that due to some size dispersion, it is difficult to define the transition temperature accurately. One may observe that the spectra indicate the persistence of the two phases for more than 50 K on each side of the transition lines α–β and β–γ.

## C. Gibbs–Thomson Relationship

The Gibbs–Thomson relationship (14) relates the lowering $\Delta T = T - T^{\circ}$, of the melting temperature to the radius (nm) of crystals:

$$\frac{\Delta T}{T^0} = \frac{2V_\alpha}{\Delta H_{\alpha-\beta}} \sigma \frac{1}{r}.$$

$V\alpha$ is the molar volume of the crystalline phase, $\Delta H_{\alpha-\beta}$ is

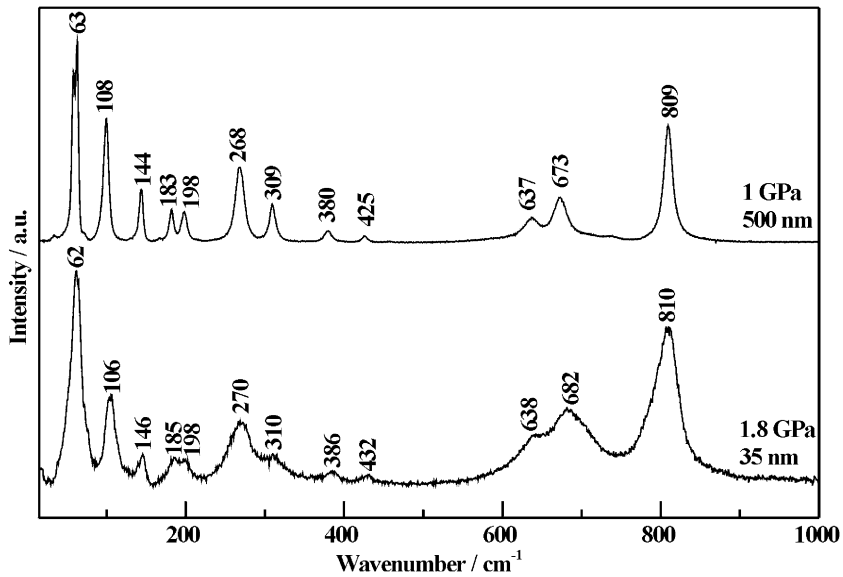


**FIG. 11.** Comparison between spectra obtained at 1 GPa for the bulk sample and at 1.8 GPa for the 35 nm sample, both spectra correspond to the *HP*1 phase of $P2_1/c$ structure.

the free molar melting enthalpy, $\sigma$ is the liquid–solid interfacial energy, and $r$ is the radius of the small crystals (in the spherical approximation). The transposition of this relationship to a solid–solid transformation is possible provided one assumes the existence of an intergranular amorphous zone extending on some interatomic distances (14).

From the above analysis, it can be concluded that high-temperature phases of the bulk $WO_3$ are found stable at much lower temperatures for nanocrystalline samples of this compound. Figure 8 sketches this statement for all samples. However, in the present state of this study, and in the absence of high-temperature diffraction studies, only the transitions observed for 60, 35 and 16 nm samples can be quantitatively compared to those of the bulk via the Gibbs–Thomson relationship. These samples at the difference with the 2 and 4 nm samples, present the advantage to be exempt of water and to be stable in a broad range of temperature and to exhibit at least one reversible transition below 800 K, i.e., at a temperature low enough for preventing the crystallite growing. If this relationship is applied to the $\beta-\alpha$ orthorhombic–tetragonal transformation of the 35 nm sample the following numerical values must be introduced: $\Delta T_{\beta-\alpha} = 1171\text{-}800 = 371$ K, $V_\beta = 21.6\,\text{cm}^3$ (27), $r = 35/2$ nm, $\Delta H_{\alpha-\beta} = 1.88$ kJ/mol (36). The interfacial energy $\sigma$ is found equal to $0.241\,\text{J/m}^2$ which is quite a reasonable value (37).

Reciprocally, using the same values for $\Delta H_{\alpha-\beta}$ and $\sigma$ as above, one can expect a temperature downshift of 810 K for the 16 nm sample and 3242 K for the 4 nm sample. This correlates well with the fact above that at ambient temperature, the tungsten oxides of these grain sizes were stabilized in high-temperature modifications.

Finally, these results confirm that the electrical properties of the 2 and 4 nm samples, measured between 300 and 500 K, which were found to be affected by shifting the atmosphere from air to $CH_4$ or CO are not due to a structural transition but only to the chemical interaction of gases. Actually, this interaction resulted in the formation of a thin film of carbon (6).

### *D. Pressure Effect*

An overview of the high-pressure Raman spectra of the different samples obtained without pressure-transmitting medium in non-hydrostatic conditions (a) and with a pressure-transmitting medium in hydrostatic conditions (b) are given in Figs. 9 and 10. Continuous loss of the whole spectrum intensity and the shift of all Raman bands to high-frequency values are observed for all the samples under hydro- and non-hydrostatic pressure.

The pressure dependence of the 35 nm samples in hydro- and non-hydrostatic conditions is similar (Fig. 9). In both cases, the decompression gives the initial structure in a few minutes. One can notice that the 31.2 GPa hydrostatic spectrum is identical to the 21.5 GPa non-hydrostatic spectrum as if there was some delay in the pressure effect for the non-hydrostatic case. Three transitions can be evidenced: one is characterized by the growth of a band at

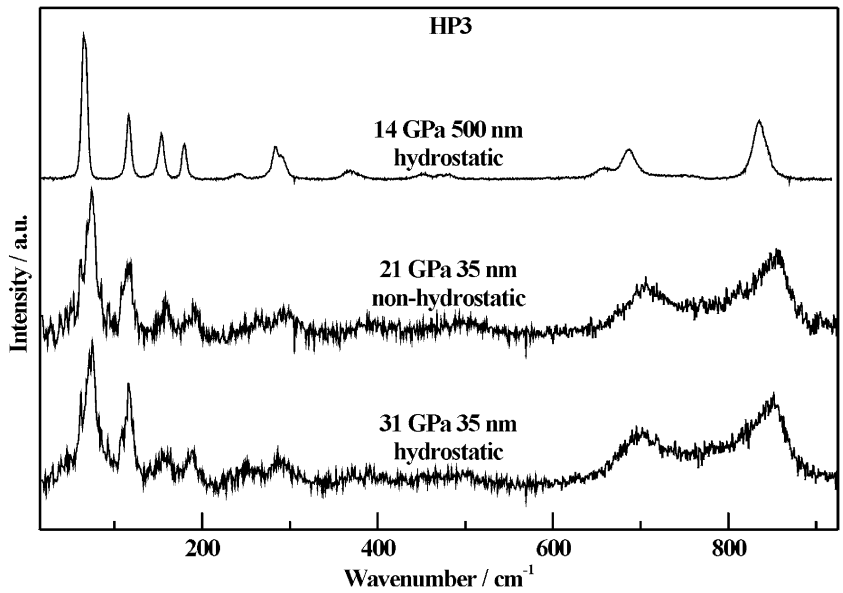


**FIG. 12.** Comparison between spectra obtained at 14 GPa for the bulk sample and at 21 and 31 GPa for the 35 nm sample, all spectra correspond to the *HP*3 phase.

about 120 $cm^{-1}$ marked with an arrow in Figs. 9a and 9b, it takes place between 1 and 2 GPa when considering both Figs. 9a and 9b. The second one may correspond to the splitting of the band at about 150 $cm^{-1}$ marked with a double arrow in the figure. The third one takes place between 25 and 35 GPa and is only visible in Fig. 9a for the non-hydrostatic case. It is identified by the quasi-disappearance of the spectrum. Because of the observed delay in the evolution of the non-hydrostatic case, this transition could occur above 35 GPa, the maximum investigated pressure in the hydrostatic case. The absence of Raman spectrum for this phase may indicate that the structure is cubic (at least at short-range order) or is strongly conductive (for explaining the non-penetration of the incident laser excitation). Note that defects generated by the elevation of temperature may induce both a structural change and an electronic mobility, this phase is noted *HPm* in Fig. 9a, to suggest that this phase might have some metallic property.

The spectra between 1.8 and 3.1 GPa for hydrostatic and between 1.1 and 9.5 GPa for the non-hydrostatic cases are quite close to those of the *HP*1 spectra obtained for the bulk $WO_3$ above 0.1 GPa in Ref. (13) and described by the $P2_1/c$ space group (12). This is clearly demonstrated by Fig. 11. Thus, it must be noted that this *HP*1 phase is induced at a higher pressure for the 35 nm sample than for the bulk $WO_3$. The second transition takes place above 3 GPa for the hydrostatic case and leads to a spectrum which is close to the *HP*3 one of the bulk $WO_3$. The poor definition of the spectra can explain that the intermediate *HP*2 phase is not evidenced, at some extent this transition can be put into correspondence with the *HP*1–*HP*2 transition in the bulk $WO_3$. Thus, one can consider that the nanometric size effect induces a shift of about 1 GPa for the first transition and of about 4–9 GPa towards high pressure for the second transition. In any case as demonstrated in Fig. 12, for obtaining with the 35 nm sample a spectrum, similar to the one obtained under 14 GPa for the bulk $WO_3$, it is necessary to raise the pressure at 21 and 31 GPa for the non-iso and hydrostatic cases, respectively. Such observations were made recently for ZnO in Ref. (38) where the shift from 9.9 to 15.1 GPa for a 12 nm sample was attributed to a surface energy difference between the two phases involved. A typical value of 11 kJ/mol was found for the surface energy difference between the two phases. Similar conclusions were also derived for CdSe, CdS and Si (39–41). The shift of the transition pressure following (38), can be written as

$$\begin{aligned} P_2 - P_1 = {} & P_1(\Delta V_1(P_1)/\Delta V_2(P_2) - 1) \\ & + (U_{2\text{surf}}(2, P_2) - U_{2\text{surf}}(1, P_2))/\Delta V_2(P_2) \\ & + ((U_1(1, P_1) - U_1(1, P_2)) - (U_1(2, P_1) \\ & - U_1(2, P_2)))/\Delta V_2(P_2), \end{aligned}$$

where 1 and 2 refer to two phases, respectively.

The $\Delta V_{\text{Bulk }12}$ was measured recently for bulk $WO_3$ (12), the same measurement of $\Delta V_{\text{Nano }12}$ is programed in a near future. The introduction of these values should permit to derive the surface energy difference between the two phases.

The pressure dependence of the 2 and 4 nm samples is similar. The broadbands in the 800 $cm^{-1}$ region lose

continuously their intensity. In the case of the 4 nm sample in a transmitting medium, one observes a spectrum change at 34 GPa. The broadband at 800 $cm^{-1}$ disappears completely while a new broadband spreading from 400 to 600 $cm^{-1}$ is observed. This state is designated by *HP*4 in Fig. 10.

## V. CONCLUSIONS

The structural changes of several nanocrystallized samples of tungsten oxide were investigated by Raman spectroscopy between 77 and 1200 K and up to 35 GPa.

The 60 nm sample at 300 K is in the $\gamma$-form and at the difference with the bulk $WO_3$ is not a mixture of $\delta$-and $\gamma$-forms. This sample starts to transform reversibly into the $\beta$-structure below 550 K instead of 623 K for bulk $WO_3$ and to the $\alpha$-structure below 950 K instead of 1171 K in bulk oxide. However, this second transformation is not completely reversible because crystallites start to grow at such high temperatures. The 35 nm sample at 300 K is in a short-range structural state close to the $\beta$-form, it transforms into the $\alpha$-form below 800 K, i.e., with a lowering of the transition temperature of 371 K. In the same way, the 16 nm sample undergoes a transition between a pseudo $\beta$-structure and the $\alpha$-form at about 700 K. The 2 and 4 nm samples are in an amorphous state in which the short-range order may be close to the $\alpha$-structure. These samples did not present a phase transition in their stability temperature range. The Gibbs–Thomson relationship has been transposed to this solid–solid transformation and has been found to deliver a reasonable value (0.241 $J/m^{-2}$) for the interfacial energy.

All the samples undergo phase transitions under a pressure increase. For the 35 nm sample, an increase of some transition pressures compared to the bulk oxide was observed. As for temperature-induced transitions, this transition-pressure shift is likely related to the role of the surface energy.

## ACKNOWLEDGMENT

E. Djurado is acknowledged for her active help in the preparation of $WO_3$ samples by spray-pyrolysis method.

## REFERENCES

1. H. Gleiter, *Acta Mater* **48,** 1 (2000).
2. A. A. Tomchenko, *Sensors Actuators B* **68,** 48 (2000).
3. A. A. Tomchenko, V. V. Khatko, and I. L. Emelianov, *Sensors Actuators B* **46,** 8 (1998).
4. M. Tong, G. Dai, and D. Gao, *Mater Chem Phys*. **69,** 176 (2001).
5. T. Jinkawa, G. Sakai, J. Tamaki, N. Miura, and N. Yamazoe, *J. Mol. Cat. A* **155,** 193(2000).
6. M. Boulova, A. Gaskov, and G. Lucazeau, *Sensors and Actuators B* **81,** 99 (2001).
7. C. Howard, V. Luca, and K. Knight, *J. Phys.: Condens. Matter* **14,** 377 (2002).
8. Y. Xu, S. Carlson, and R. Norrestam, *J. Solid State Chem*. **132,** 123 (1997).
9. P. M. Woodward, A. W. Sleight, and T. Vogt, *J. Solid State Chem*. **131,** 9 (1997).
10. K. R. Locherer, I. P. Swainson, and E. K. H. Salje, *J. Phys.: Condens. Matter* **11,** 4143 (1999).
11. K. R. Locherer, I. P. Swainson, and E. K. H. Salje, *J. Phys.: Condens.Matter* **11,** 6737 (1999).
12. P. Bouvier, M. Boulova, and G. Lucazeau, *J. Phys.: Condens. Matter* **14,** (2002).
13. M. Boulova, N. Rosman, and G. Lucazeau, *J. Phys.: Condens. Matter* **14,** (2002).
14. P. J. Desre, *Nanostruct. Mater*. **8,** 687 (1997).
15. P. Bouvier, H. C. Gupta, and G. Lucazeau, *J. Phys. Chem. Solids* **62,** 873 (2001).
16. P. Bouvier, E. Djurado, G. Lucazeau, and T. LeBihan, *Phys. Rev. B* **62,** 8731 (2000).
17. P. Perriat, J. C. Niepce, and G. Caboche, *J. Thermal Analysis* **41,** 635 (1994).
18. E. Djurado and E. Meunier, *J. Solid State Chem*. **141,** 191 (1998).
19. C. H. MacGillary, G. D. Rieck, G. K. Williamson, and W. H. Hall, Int. Tables X-ray Crystallogr. **3,** 318 (1962).
20. Williamson and Hall, *Acta Metall*. **1,** 22 (1953).
21. G. J. Priermarini, S. Block, J. D. Barnett, and R. A. Forman, *J. Appl. Phys*. **46,** 2774 (1975).
22. E. Salje, *Acta Crystallogr. A* **31,** 360 (1975).
23. E. Salje, *Acta Crystallogr. B* **33,** 574 (1977).
24. E. Salje and G. Hoppmann, *High Temp. High Pressures* **12,** 213 (1980).
25. E. Cazzanelli, C. Vinegoni, G. Mariotto, A. Kuzmin, and J. Purans, *J. Solid State Chem*. **143,** 24 (1999).
26. E. Cazzanelli, C. Vingeoni, G. Mariotto, A. Kuzmin, and J. Purans, *Solid State Ionics* **123,** 67 (1999).
27. T. Vogt, P. M. Woodward, and B. A. Hunter, *J. Solid State Chem*. **144,** 209 (1999).
28. T. Pagnier, M. Boulova, A. Galerie, A. Gaskov, and G. Lucazeau, *J. Solid State Chem*. **143,** 86 (1999).
29. T. Pagnier, M. Boulova, A. Galerie, A. Gaskov, and G. Lucazeau, *Sensors Actuators B* **71,** 134 (2000).
30. L. Abello, B. Bochu, A. Gaskov, S. Koudryavtseva, G. Lucazeau, and M. Roumyantseva, *J. Solid State Chem*. **135,** 78 (1998).
31. F. Cora and C. R. A. Catlow, *Faraday Discuss*. **114,** 421 (1999).
32. A. Dieguez, A. Romano-Rodriguez, A. Vila, and J. R. Morante, *J. Appl. Phys*. **90,** 1550 (2001).
33. L. Saviot, B. Champagnon, E. Duval, and A. I. Ekimov, *J. Cryst. Growth* **184,** 370 (1998).
34. L. Saviot, B. Champagnon, E. Duval, I. A. Kudryavtsev, and A. I. Ekimov, *J. Non-Cryst. Solids* **197,** 238 (1996).
35. E. Duval, A. Boukenter, and B. Champagnon, *Phys. Rev. Lett*. **56,** 2052 (1986).
36. G. V. Samsonov, Physico-chemical properties of oxides, *in* "Handbook Metallurgy," 3rd ed., p. 91, Moscow, 1978.
37. P. Bouvier, Thesis of the Institut National Polytechnique de Grenoble, 2000.
38. J. Z. Jiang, J. S. Olsen, L. Gerward, D. Frost, D. Rubie, and J. Peyronneau, *Europhys. Lett*. **50,** 48 (2000).
39. S. H. Tolbert and A. P. Alivisatos, *Science* **265,** 373 (1994).
40. S. H. Tolbert and A. P. Alivisatos, *J. Chem. Phys*. **102,** 4642 (1995).
41. S. H. Tolbert, A. B. Herhold, L. E. Brus, and A. P. Alivisatos, *Phys. Rev. Lett*. **76,** 4385 (1996).